Ab Initio Study of the Sodium Intercalation and Intermediate Phases in Na$_{0.44}$MnO$_2$ for Sodium-Ion Battery

Heejin Kim,[†] Dong Jun Kim,[‡] Dong-Hwa Seo,[§] Min Sun Yeom,[#] Kisuk Kang,[§] Do Kyung Kim,[‡,*] and Yousung Jung[†,*]

[†]Graduate school of EEWS (WCU) and [‡]Department of Materials Science and Engineering, KAIST, Daejeon 305-701, Republic of Korea

[§]Department of Materials Science and Engineering, Seoul National University, Seoul 151-742, Republic of Korea

[#]Industrial Supercomputing Department, SMB Knowledge Support Center, KISTI, Daejeon 305-806, Republic of Korea

S *Supporting Information*

ABSTRACT: The Na$_{0.44}$MnO$_2$ structure is a promising cathode material for sodium ion batteries due to a high capacity (~130 mAh/g) and good cycle performance. In this work, we present the results of density functional theory (DFT) calculations on the structural and electrochemical properties of Na$_{0.44}$MnO$_2$, combined with experiments. Seven intermediate phases and the two-phase reactions among them were found, where the calculated voltage profile agreed well with experiments. We found that the S-shaped tunnel is not empty in the deintercalated Na$_{0.22}$MnO$_2$ structure but has a partial occupancy of sodium ions. The new sodium sites were found in a limited sodium composition range (x = 0.44−0.55) which is attributed to the electrostatic interactions between sodium ions and manganese atoms. The asymmetric lattice evolution in Na$_{0.44}$MnO$_2$ as a function of sodium insertion/deinsertion is shown to be due to the Jahn−Teller effects. On the basis of this interpretation, we suggest that the Cr substitution will reduce the volume change significantly.

KEYWORDS: *sodium ion batteries, density functional theory, sodium manganese oxide, insertion/deinsertion mechanism, Jahn−Teller distortion*
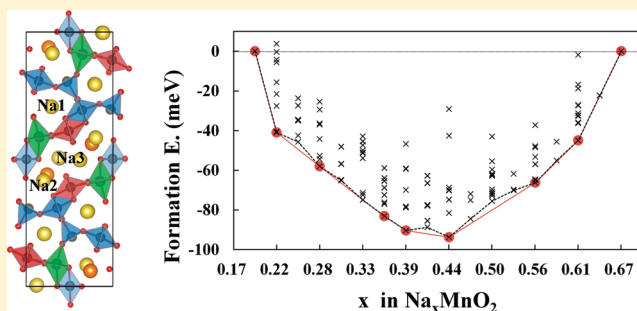
1. INTRODUCTION

Heretofore, the research on rechargeable batteries has largely focused on the gravimetric and volumetric capacity since so far the batteries have been mainly used in small devices where the size and weight are important. Recently, the large scale applications such as electric vehicles or smart grid systems have become a new frontier of rechargeable batteries together with the global environmental issues. In such a large scale system, the cost of materials (manufacturing cost) and the cycle performance (maintenance cost) are as important as fundamental characteristics. These demands on the lower cost electrode materials led to a rediscovery of sodium ion batteries in recent years.[1−11] In spite of many similarities between lithium and sodium ions, their battery characteristics can be quite different. For example, electrochemically inactive structures toward lithium ions such as a layered chromium dioxide can be an active material for sodium ions[6] since the size difference between the two alkali ions makes each ion have a different stability within the same structure.[12] Therefore, detailed investigations on the potential electrode materials for sodium ions are necessary.[13]

Among various cathode materials for sodium ions, the Na$_{0.44}$MnO$_2$ compound shows several outstanding properties:

(1) It has a capacity of 120−130 mAh/g in experiments,[9,10] which is one of the highest capacities among the existing sodium ion batteries. (2) The nanosized Na$_{0.44}$MnO$_2$ shows a good cycle performance with 77% capacity retention after 1000 cycles.[9] (3) It is applicable in aqueous electrolyte[11] which means that a substantial reduction of cost is additionally possible. Despite all these favorable characteristics of Na$_{0.44}$MnO$_2$, however, the underlying mechanism of extraction processes and the structures of intermediate phases during the electrochemical cycles of this material and the analogous Li$_{0.44}$MnO$_2$ are largely unknown. In this work, we study the electrochemical and structural properties of Na$_{0.44}$MnO$_2$ using the first principles calculations and present the detailed charging/discharging processes that are not easily addressable in experiments.

2. COMPUTATIONAL AND EXPERIMENTAL METHODS

We performed the spin-polarized density functional theory (DFT) calculations using the Vienna Ab initio Simulation Package (VASP)[14]

with the projector-augmented wave (PAW)[15] pseudopotentials. The Perdew−Burke−Ernzerhof (PBE)[16] exchange-correlation functional is used with the Hubbard U-corrections in the rotationally invariant form introduced by Dudarev et al.[17] to address the self-interaction energy. The effective single parameters $U-J$ of 3.9 eV, 3.5 eV, 2.5 eV, and 3.1 eV were used for Mn, Cr, Ti, and V, respectively, based on the Wang et al.'s approach and its applications.[18−20] All total energy calculations were performed with ($a \times b \times 4c$) supercells of 9.2 Å × 26.7 Å × 11.5 Å for 72 formula units (f.u.) of $Na_{0.44}MnO_2$, including 248 atoms total in a calculation cell. This rather large cell size is used to investigate the energetic stability of various sodium configurations. A plane-wave basis with an energy cutoff of 500 eV was used and a 2 × 2 × 2 Monkhorst-Pack[21] k-points mesh was sampled for the well converged energy values. To calculate the lowest formation energies of various compositions, 20 lowest electrostatic energy configurations of sodium ions determined using the Ewald summation technique[22] were used as an input for ab initio geometry optimizations at each composition.

All calculations were performed in a ferromagnetic (FM) ordering since the FM arrangements give lower energies than antiferromagnetic (AFM) arrangements in all composition ranges of Na_xMnO_2 ($x = 0.22-0.66$). In experiments, only the magnetic properties of isostructural $Li_{0.44}MnO_2$ are recently reported to have a weak FM ordering due to the AFM core and FM shell structures.[23] However, the electrochemical properties of the large particles[10] (500 nm diameter) with relatively small surface area to volume ratio and hence the AFM-rich samples and those of the smaller particles[9] (50 nm diameter) with large surface area and hence the FM-rich samples were almost identical, implying that the magnetic structure has an insignificant effect on the electrochemical properties of $Na_{0.44}MnO_2$. The calculated crystal structures were visualized using the program VESTA.[24]

Sodium manganese oxide electrode materials were synthesized by the modified Pechini process. All metallic source, sodium acetate, and manganese acetate were dissolved in DI water and mixed with citric acid. The transparent solution was heated until sufficient water had evaporated, and a gel was obtained. The gel was heated to dry and calcined to remove organic binders. The calcined powder was heat treated at 300 °C for 8 h. The preheated treated sample was ground and heat treated at 800 °C for 9 h. Heat treatments were carried out under air condition. For electrochemical measurement, synthesized sodium manganese oxide was used for working electrode and metallic sodium was used for counter electrode to make a Na-half cell. The weight percent of active material was 75 wt % active materials, 18 wt % conductive carbon black, and 7 wt % organic binder. The active material was made into a slurry and casted on aluminum foil. The electrode samples were dried in a vacuum oven overnight. The electrolyte was 1 mol/L $NaClO_4$ dissolved in a mixture of EC and DMC (1:2 by weight), and the separator was a microporous membrane (Celgard 2400). The cells were assembled in an argon-filled glovebox and 2032 type coin cells were used for the characterization. All electrochemical measurement was characterized using Biologic VMP3 instruments at room temperature. The XRD pattern and SEM image of as-synthesized $Na_{0.44}MnO_2$ particles are presented in Figure S1 (Supporting Information).

3. RESULTS

3.1. Crystal Structure of $Na_{0.44}MnO_2$. The crystal structure of $Na_{0.44}MnO_2$ is isostructural with $Na_4Mn_4Ti_5O_{18}$ which was first reported by Mumme in 1968 and belongs to the space group *Pbam* with orthorhombic structure.[25,26] Among the five crystallographic sites for metal atoms shown in Figure 1a, the Mn1, Mn3, and Mn4 sites are occupied by Mn^{4+} (Ti^{4+} in $Na_4Mn_4Ti_5O_{18}$) while the Mn2 and Mn5 sites are occupied by Mn^{3+}. The square pyramidal Mn5 sites may be viewed as hinges to relieve lattice strains and changes that occur during insertion/extraction of sodium ions.[27] For sodium ions, there are three binding sites (Na1, Na2, and Na3 in Figure 1) by symmetry consideration where it has been proposed that the Na1 site in the small tunnel is almost fully filled while the other
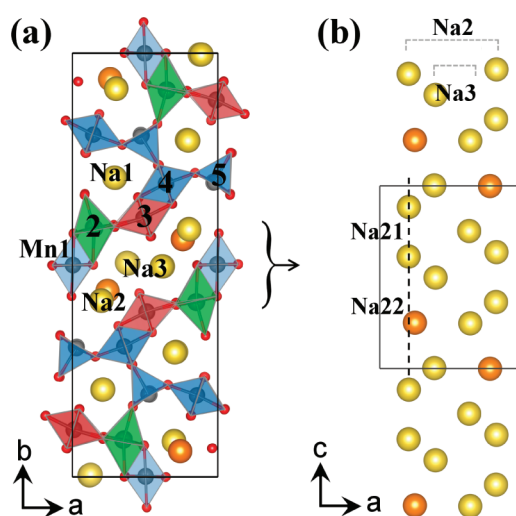

Figure 1. (a) Crystal structure of $Na_{0.44}MnO_2$ with five crystallographic sites for manganese and three sites for sodium ions. (b) The most probable sodium configuration is in the S-shaped tunnel along the c-axis where the Na2 site has two different sodium positions, Na21 and Na22.

sites (Na2 and Na3) in the S-shaped tunnel are approximately half-filled.[10,28] Recently, more detailed atomic arrangements for $Na_{0.44}MnO_2$ were obtained from the single-crystal X-ray diffraction (XRD)[29] and the synchrotron radiation diffraction measurements.[30] The spatial configurations of sodium and manganese atoms were also shown to be temperature dependent[30] where the number of distinguishable sodium sites increased from 3 at 500 K to 8 at 5 K temperature. On the other hand, Chu et al.'s measurements[29] at room temperature identified four unique sodium sites due partly to the above-mentioned temperature effects as well as the inferior resolution of conventional XRD experiments.

In this work, we calculated the minimum energy configurations (most stable Na sites for a given stoichiometry) for $Na_{0.44}MnO_2$ and found that the structure shown in Figure 1b is the lowest energy structure for sodium ions in the S-shaped tunnel. We found that the Na2 sites are further split into two slightly displaced but distinct environments (with different coordination orientation as described below), denoted as Na21 (yellow) and Na22 (orange) in Figure 1b. Na22 is displaced to an inner side of the S-shaped tunnel relative to the Na21 site. The occupancies of Na1, Na21, Na22, and Na3 being 0.75, 0.5, 0.25, and 0.5, respectively, are consistent with the refinement results of XRD experiment[29] except that the Na1 site is calculated to have less occupancy (0.75 in calculation vs 0.92 in experiment) due to a limited size of the model structures used in our calculations.[31]

Sodium ions in the Na2 sites have a trigonal prismatic coordination with the Na−O bond distance of 2.3−2.4 Å, but Na21 and Na22 have a different relative orientation. Na21 faces toward Na3 sites with one edge-sharing while Na22 is in the opposite orientation sharing two edges with Na3. Since all Na3 sites are occupied in the $Na_{0.66}MnO_2$ as in Figure 2a, the Na22 sites cannot be occupied due to a high electrostatic repulsion experienced by nearby Na3 ion. Since the vacancies are produced in the Na3 sites during the extraction of sodium ions from $Na_{0.66}MnO_2$, the occupation of Na22 sites is prompted as shown in Figure 2b in $Na_{0.44}MnO_2$. The coordination of two different Na2 sites (Na21 and Na22) in $Na_{0.44}MnO_2$ is
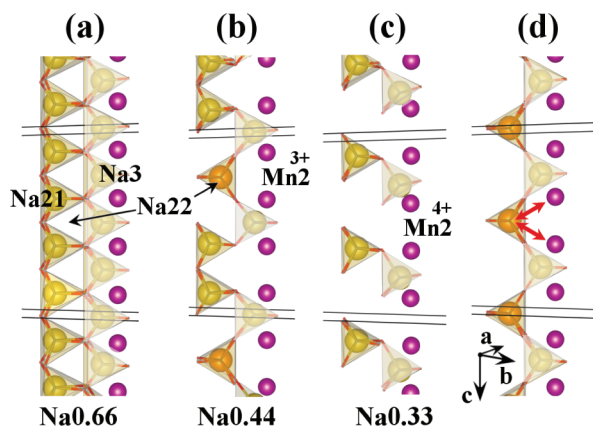
Figure 2. (a) Two different Na21 and Na22 sites are identified from their relative orientation of trigonal prismatic coordination and (b) the Na22 site can be prompted by the vacancies at Na3 sites. (c) Below the Na$_{0.44}$ composition, the Na21 site is more stable than the Na22 site due to the (d) unfavorable interaction between Mn^{4+} and Na$^+$ ion.

consistent with the experimental sodium positions at room temperature[29] and the low temperature synchrotron measurements.[30] In further deintercalated structures than the Na$_{0.44}$MnO$_2$, the Na21 sites (Figure 2c) are calculated to be more favorable than the Na22 sites (Figure 2d). This result is attributed to the selective change in oxidation states of Mn2 from 3+ to 4+ during the deinsertion process. The repulsive interaction between Mn^{4+} and Na$^+$ ions[30] elongates the distance between Mn2 and Na2; hence, the Na21 sites with longer Mn−Na distance ($d = 4.52$ Å) become more stable than Na22 sites ($d = 4.24$ Å). A specific sequence of oxidation/reduction of manganese sites will be discussed in Section 3−3 in more detail.

3.2. Sodium Deintercalation Mechanism. Consecutive two-phase reactions are observed in our charging and discharging experiments of Na$_{0.44}$MnO$_2$, consistent with previous reports.[9,10] Although the Na$_{0.44}$MnO$_2$ structure has a significant number of Mn^{3+} ions for the entire range of electrochemical cycles, it does not undergo transformations to other structures, since (1) the oxygen lattice of Na$_{0.44}$MnO$_2$ is not cubic close packed, but rather the rippled close packed layers are stacked along the a-axis (Figure S2, Supporting Information). Although there are other types of sodium manganese oxides such as Na$_{0.4}$MnO$_2$ and Na$_{0.7}$MnO$_{2+y}$,[25,32] these structures are quite different from Na$_{0.44}$MnO$_2$ and thus significant structural rearrangements should occur for transformation. (2) The transformation to the spinel, a known problem in lithium manganese oxides,[32,33] also does not occur in Na$_{0.44}$MnO$_2$ due to a size mismatch between sodium and manganese[34] as well as the aforementioned different oxygen frameworks. (3) Moreover, the manganese migration into the adjacent vacant sodium site is unfavorable (Table S1, Supporting Information), and (4) the Na$_x$MnO$_2$ ($x = 0.22$ to 0.66) structures are energetically more stable than the nearby Na−Mn−O compounds (Figure S3, Supporting Information).

Therefore, the observed biphasic phenomena are not attributed to the evolution of new structures, consistent with the in situ XRD measurements that the phases observed during electrochemical cycles are structurally very close.[10] The charge ordering, rather than sodium ordering, may then be a possible source of biphasic phenomena[35] since there was no evidence to indicate long-range ordering of sodium ions in HRTEM and

XRD experiments.[10,29] However, both charge and sodium orderings could also be coupled[36] since the electrostatic interaction between Na$^+$ and Mn^{4+} is clearly different than that between Na$^+$ and Mn^{3+}. The plateau between $x = 0.44$ and 0.55 compositions may, however, be primarily due to the splitting of the Na2 sites as described below.

Figure 3 shows the calculated formation energies and a consequent voltage profile[37] obtained along the minimum
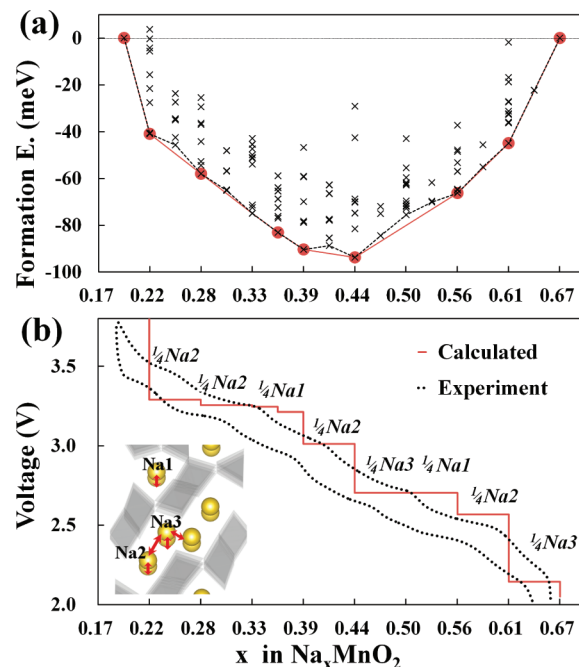
Figure 3. (a) Formation energies ($\times$) calculated from the 156 different sodium configurations indicate seven stable intermediate phases during the cycles of Na$_x$MnO$_2$ ($x = 0.19−0.44$). (b) The calculated voltage profile along the minimum energy path of formation energies, red line of (a), agree well with the first charging/discharging experiment (0.1 C). The extracted sodium sites for each voltage plateaus are denoted. For example, a quarter of Na3 sites are extracted from Na$_{0.66}$ to Na$_{0.61}$ at 2.15 V.

energy structures as illustrated in Figure S4 (Supporting Information). Note that there are several structures with different sodium configurations that are energetically quite close for each composition (1−12 meV per formula unit) which could lead to a mixture of various local configurations with similar stability without crystallographic long-range ordering in experiments.[29] The computed voltage plateaus in Figure 3b agree well with the first charging profile of experiments with two longer plateaus (2.71 V and 3.22 V) and four shorter plateaus (2.15 V, 2.55 V, 3.01 V, and 3.27 V). Some discrepancies are seen in the low sodium concentration region, especially for deintercalation from Na$_{0.22}$MnO$_2$ to Na$_{0.19}$MnO$_2$ (4.4 V in calculation and 3.5−4.0 V in experiment). As we discuss it in more detail in Figure 4, it may be due to a different characteristic of sodium deintercalation from Na$_{0.22}$MnO$_2$ to Na$_{0.19}$MnO$_2$ (where the electrons of mainly oxygen 2p character are largely involved for redox couple) as compared to all the other compositions (where only the localized Mn-3d electrons are involved), and their descriptions using a single empirical parameter DFT+U method.

The formation energies are calculated in reference to the Na$_{0.19}$MnO$_2$ and Na$_{0.66}$MnO$_2$. The seven intermediate phases

are identified from our calculations (red circles in Figure 3a), consistent with XRD measurements where at least six phases were identified.[9,10] The overall sequence of sodium extraction was Na3, Na2, and then Na1 as denoted in Figure 3b. It can be understood qualitatively from the electrostatic repulsion between sodium ions. As illustrated in the inset of Figure 3b, sodium ions in the Na3 sites experience repulsion from those in its own channel (d = 2.91 Å) and neighboring Na2 (d = 3.31 Å) and Na3 (d = 2.87 Å) sites. On the other hand, sodium ions in the Na2 sites encounter repulsion from those in its own channel (d = 2.91 Å) and the nearby Na3 sites (d = 3.31 Å). Likewise, sodium ions in the Na1 sites experience the repulsion only from those in its own channel (d = 2.91 Å). Therefore the sodium ions in Na3 sites with the strongest repulsion are first deintercalated, and then the Na2 and Na1 sites are extracted sequentially. These can be schematically captured by the number of arrows (repulsive interactions) and their lengths (distances of each such interaction). Since the distance between Na ions in the same channel and the Na3−Na3 distance is relatively small or comparable compared to the sum of vdW radii of sodium ions (2.82 Å[38]−3.03 Å[39]), there may be additional Pauli repulsion for such pairs due to the orbital overlap.

The Na22 sodium sites identified in the previous section were found only in between $Na_{0.44}MnO_2$ and $Na_{0.55}MnO_2$ due to the unfavorable electrostatic repulsion from the neighboring cations as mentioned in a previous section. This extended biphasic region between $Na_{0.44}MnO_2$ and $Na_{0.55}MnO_2$ can be a significant source of the capacity fading compared to the other two-phase regions since (1) the sodium ion diffusion is slower in this region[9] and (2) the other nonequilibrium reaction pathways[40] may be more difficult in this region due to the relatively high energies of intermediate states as shown in Figure 3a. From these results, we can explain the experimental finding that the capacity is faded at the low potential operation[10,41] while the cycle performance is enhanced when the low potential operation is excluded[11,41] or when the nanosized electrode is utilized[9] which has a tolerance to the diffusion problem. In addition, a significant capacity fading (∼50%) on the first cycle was observed for nanosized samples,[9] implying some unknown surface reactions on the first cycle are also responsible for the capacity fading.

The structure of $Na_{0.22}MnO_2$ is therefore the $Na1_{0.11}Na3_{0.11}MnO_2$, in our calculations, contrary to a previous suggestion that the complete removal of sodium ions only in the S-shaped tunnels (both Na2 and Na3) leads to a $Na_{0.22}MnO_2$ composition.[10,28] Further verifications of the calculated intermediate structures are discussed in the following discussion of electrochemical measurements and the lattice parameter evolution in the next section.

In spite of the oxidation states of Mn1−Mn4 being already 4+ in $Na_{0.22}MnO_2$, further deintercalation up to the $Na_{0.19}MnO_2$ is observed in our experiments, consistent with previous reports.[9,10] It implies that in $Na_{0.19}MnO_2$, the oxidation states of Mn1−Mn4 should be higher than 4+, or the remaining Mn^{3+} at Mn5 should be oxidized to Mn^{4+}, or else the additional electrons should be displaced from oxygen for charge neutrality. To understand this maximum charging composition ($Na_{0.19}MnO_2$), we analyzed the electronic structure of Mn and O at the $Na_{0.44}MnO_2$ and $Na_{0.22}MnO_2$ composition. Figure 4 shows the local density of states (LDOS) near the Fermi level including the highest occupied molecular orbital (HOMO) and the lowest unoccupied molecular orbital
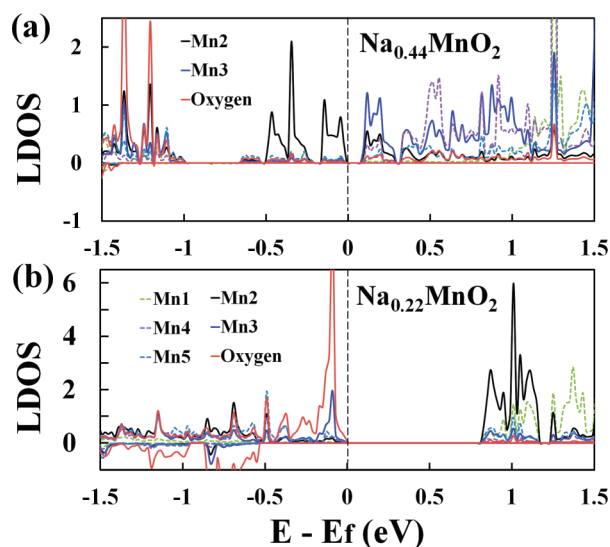

Figure 4. (a) Relevant redox couple for oxidation of $Na_{0.44}MnO_2$ is the Mn_{3d} orbital of Mn2 (black line) with only a marginal involvement of oxygen component. For reduction from $Na_{0.44}MnO_2$, however, the added electrons will likely go to the Mn3 sites (blue line) due to a larger density of the unoccupied states near the Fermi level. (b) For further oxidation of $Na_{0.22}MnO_2$, the mixed but primarily anionic p character (O-2p + Mn-3d) orbital acts as a redox couple. For reduction of $Na_{0.22}MnO_2$, the Mn2 sites (black line) will likely accept additional electrons.

(LUMO) regions since these regions are where the most interesting chemistry occurs upon charging and discharging. As shown in Figure 4a, the charging process from $Na_{0.44}MnO_2$ to $Na_{0.22}MnO_2$ which involves the oxidation of Mn2 from Mn^{3+} to Mn^{4+} (Figure 7) requires a removal of electrons in the HOMO that are mostly e_g orbital character of Mn2 (black line). On the other hand, in the $Na_{0.22}MnO_2$ (Figure 4b), the HOMO is a mixture of pinned t_{2g} orbital of Mn3 (blue line) and O-2p orbital (red line), and these mixed O-2p + Mn-3d orbitals with primarily O-2p character act as a redox couple for charging from $Na_{0.22}MnO_2$ to $Na_{0.19}MnO_2$. The further oxidation beyond $Na_{0.19}MnO_2$ would then be restricted by an *intrinsic voltage limit* of pinning concept introduced by Goodenough and Kim.[42] The oxidation states of Mn5 were unchanged in our calculation.

3.3. Lattice Parameter Change. The degree of volume change can be another important factor for cycle performance especially in the materials with two-phase reactions since those reactions induce some strain at the interface between the two phases.[43] Shin and Manthiram[44] also reported that the amount of capacity loss is proportional to the difference in lattice parameters between the two phases. Therefore, understanding the mechanism of lattice parameter changes during the electrochemical cycle is a plausible starting point to enhance cycle performance of the cell.

For $Na_{0.44}MnO_2$, an interesting asymmetric change of lattice parameters during the charging and discharging processes has been reported by Sauvage et al.,[10] and we provide some interpretation for these measurements in this section. During the insertion of sodium ions from the $Na_{0.22}MnO_2$ to $Na_{0.44}MnO_2$, the lattice expanded along the b-axis only, whereas a further insertion from $Na_{0.44}MnO_2$ to $Na_{0.66}MnO_2$ led to an expansion along the a- and c-axes with the b-axis unaltered. We therefore compared the calculated lattice parameters with those

obtained experimentally as a function of sodium composition. As shown in Figure 5, although the absolute lattice parameters
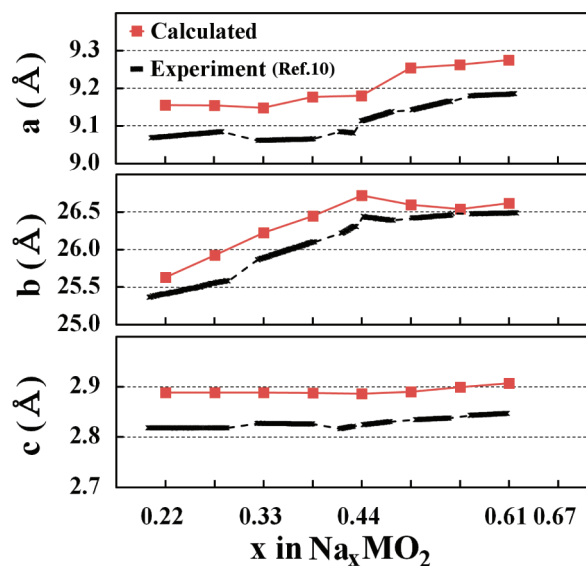

Figure 5. Insertion of sodium ions from $Na_{0.22}$ to $Na_{0.44}$ composition extends the cell along the *b*-axis only, whereas the insertion from $Na_{0.44}$ to $Na_{0.66}$ expands the cell along the *a*-axis and *c*-axis while the *b*-axis is unchanged. This asymmetric change of lattice parameters is attributed to the Jahn−Teller distortion of manganese octahedron. The experimental values are taken from ref 10.

calculated using structures obtained in Figure 3 are slightly overestimated compared to experiments, the overall asymmetric trends are well reproduced. Moreover, a noticeable split of the (350) peak in the XRD spectra upon deintercalation is also clearly identified in our simulated diffraction pattern[45] using the same calculated structure (Figure S5, Supporting Information). The overprediction of lattice parameters using DFT+U calculations has also been reported previously for various lithiated structures.[46]

To understand these asymmetric lattice changes with various sodium compositions, we investigated the change of oxidation states for each manganese atom during the discharging process. In the $Na_{0.22}MnO_2$, only square pyramidal Mn5 sites carry Mn^{3+} while all the other manganese atoms are in the Mn^{4+} state. As sodium ions are intercalated, additional electrons are localized preferentially in Mn2 sites, green atoms in Figure 1a; thus, the oxidation states of Mn2 atoms change from 4+ to 3+. This added electron occupies the d_z^2 orbital (Figure 6) and induces a strong Jahn−Teller distortion along the *z*-direction, resulting in elongation along the *b*-axis in Figure 1a. Subsequently, Mn3 sites (red atoms) are reduced from 4+ to 3+ during the sodium insertion from $Na_{0.44}MnO_2$ to $Na_{0.66}MnO_2$, leading to an evolution of lattice parameter along the *a*-axis in the same manner. In a fully discharged structure, all Mn^{3+} are changed to have square pyramidal coordination in $Na_{0.66}$ composition, attributed to a larger split of e_g bands. These results are clearly verified from the LDOS of each manganese atom (Figure 6). The change in net magnetic moments of the transition metal (TM) also confirms this sequential order of reduction.[47] Manganese in the high-spin state has a net moment of around 3 and 4 for Mn^{4+} and Mn^{3+}, respectively, in proportion to the number of unpaired electrons. Figure 7 shows that all Mn2 atoms are first reduced from Mn^{4+}
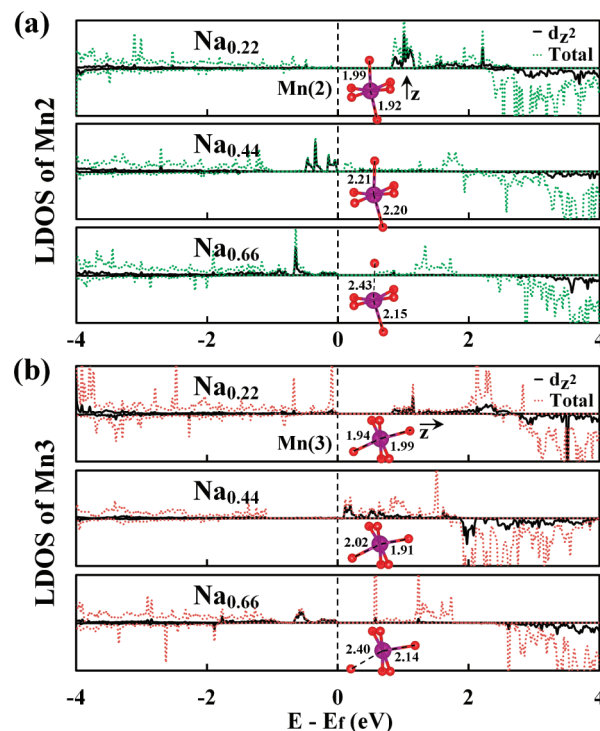
Figure 6. (a) For sodium insertion from $Na_{0.22}$ to $Na_{0.44}$, the added electrons fill the d_z^2 orbital of manganese at Mn2, inducing the elongation of lattice parameter along the *b*-axis. (b) Further insertion from $Na_{0.44}$ to $Na_{0.66}$ adds in electrons to the d_z^2 orbital of the Mn3 sites and stretches the lattice along the *a*-axis.
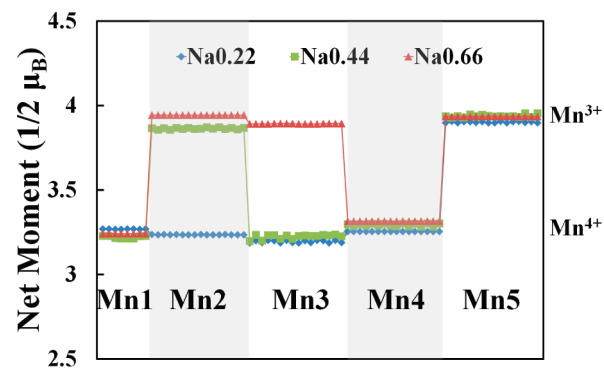
Figure 7. Change of magnetic moments during charging/discharging as a function of different Mn sites. Only Mn2 and Mn3 sites change their oxidation states between $Na_{0.22}$ and $Na_{0.66}$ compositions. All manganese at the Mn2 sites is reduced from Mn^{4+} at $Na_{0.22}MnO_2$ to Mn^{3+} at $Na_{0.44}MnO_2$. Successively, all manganese at the Mn3 sites is reduced up to $Na_{0.66}MnO_2$.

at $Na_{0.22}$ to Mn^{3+} at $Na_{0.44}$ composition. After that, all Mn3 atoms are reduced to Mn^{3+} at $Na_{0.66}$ composition.

This particular order of reduction can also be inferred from the LDOS for each manganese site. In the LDOS of $Na_{0.22}MnO_2$, Figure 4b, manganese at the Mn2 sites (black line) has the largest density of the LUMO states, indicating that additional electrons (upon sodium insertion) will most likely occupy these Mn2 sites. In the same manner, manganese at the Mn3 sites (blue line) has the largest density of the LUMO states at the $Na_{0.44}MnO_2$ composition (Figure 4a); hence, the Mn3 will be reduced for further sodium intercalation.

The other factors such as a repulsion between sodium ions in the S-shaped tunnel can affect the lattice parameters as proposed by Chu et al.[29] To study the electrostatic vs Jahn−Teller effects on the evolution of lattice parameters, we examined the volume change as a function of TM substitution without Jahn−Teller effect in their oxidation states of 3+ and 4+ such as Ti, V, and Cr. A possible degree of substitution is more likely 11%, 22%, 33%, 44%, or 55% of available metal sites according to the number of crystallographic sites. We considered the 22% and 44% substitutions in this study.

We investigated all possible TM substitution sites, and Figure S6 (Supporting Information) illustrates the most stable structure of each element for $Na_{0.44}$ composition. The most stable sodium configurations for charged/discharge states of all TM substituted compounds were identical to those of the pristine Mn compound. In the case of 22% substitution, Ti and V were preferentially located in the Mn^{4+} sites with an oxidation state of 4+, while Cr was substituted in Mn^{3+} sites, especially in Mn1 with oxidation state of 3+. For 44% substitution, additional Ti, V, and Cr are substituted in Mn^{4+} sites with an oxidation state of 4+. Although the energetically favorable substitution sites are different for each element perhaps as expected, this substitution experiment in silico enables us to clarify the Jahn−Teller effect vs the electrostatic effects between sodium ions.

The volume changes for different substituents are summarized in Figure 8. The initial volume of Ti substituted
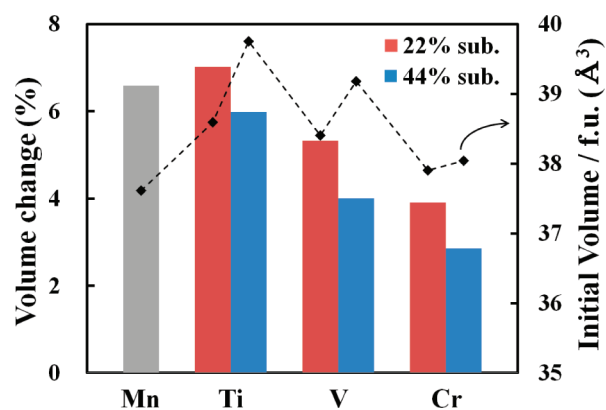
Figure 8. Calculated volume change (bar graph) as well as absolute initial volume (dotted line) as a function of metal substitution, in reference to $Na_{0.44}MnO_2$ (gray bar). The chromium substituted compounds show the lowest volume expansion since the Cr^{3+} and Cr^{4+} do not cause the Jahn−Teller distortion.

compound, $Na_x(MnTi)O_2$, is larger than the pristine manganese oxide, Na_xMnO_2, due to the larger size of Ti^{4+} ions,[48] consistent with experiments.[27] If the electrostatic repulsions between sodium ions were the major reason for the lattice evolution, the volume change of $Na_x(MnTi)O_2$ should be expected to be smaller than the Na_xMnO_2 since the distance between sodium sites is larger in $Na_x(MnTi)O_2$ than in Na_xMnO_2 (Table S2, Supporting Information). The calculated volume change in Figure 8 does not support this argument. Similarly, $Na_x(MnCr)O_2$ with chromium substitution has a comparable initial volume to Na_xMnO_2 with similar Na−Na distances, but the calculated volume evolution in Figure 8 shows a much smaller volume change in the Cr-substituted compound as compared to the pure Mn-based

compound. We show below that it can be understood using Jahn−Teller distortion.

Since the Ti is a spectator ion in $Na_x(MnTi)O_2$ that is not reduced or oxidized during sodium insertion, the Jahn−Teller distortion of manganese will still occur fully and thus the volume expansion of $Na_x(MnTi)O_2$ is similar to that of Na_xMnO_2. In the case of V-substitution, however, since the oxidation states of both Mn and V are changed during charging and discharging processes, the volume change in this complex is smaller (due to V) than that in the Ti-substituted compound, but it is still noticeable (due to Mn). For Cr-substitution, the Cr atoms are reduced and oxidized before the manganese atoms react with respect to the sodium insertion and extraction. The Cr^{3+} and Cr^{4+} do not cause the Jahn−Teller distortion since the electronic configurations are believed to have t_{2g}^3-e_g^0 and t_{2g}^2-e_g^0, respectively. Therefore, this complex shows only a half of the volume expansion during sodium intercalation as compared with the pristine manganese oxide compound. The specific sequence of redox reactions between each element described above has been determined by calculating the net magnetic moments of each metal site as a function of sodium insertion and is summarized in Figure S7 (Supporting Information). On the basis of these results, we can conclude that the Jahn−Teller distortion is a key source of the volume change in $Na_{0.44}MnO_2$.

4. CONCLUSION

We studied the sodium insertion/deinsertion mechanisms of $Na_{0.44}MnO_2$ using ab initio calculations, combined with experiments. The electrochemical and crystallographic characteristics such as voltage profile and lattice parameters evolution using the calculated structures agreed well with experiments. We found that the different coordination orientation of sodium polyhedron leads to the two different Na2 sites in S-shaped tunnels of the $Na_{0.44}MnO_2$ as observed in experiments. The competition of electrostatic interactions between sodium ions and Mn^{4+} atoms causes the Na22 sites to be occupied only in between $Na_{0.44}MnO_2$ and $Na_{0.55}MnO_2$ compositions. We clarified the sodium insertion/extraction mechanisms in $Na_{0.44}MnO_2$ and identified seven intermediate phases in detail that were observed in previous and current experiments but not characterized before. The particular order of sodium extraction could be qualitatively understood by the electrostatic interactions between sodium ions as well as some Pauli repulsion for those sodium pairs that are relatively close. We suggest that the relatively unstable intermediate phases in the long-ranged, slow-diffused biphasic region between $Na_{0.44}MnO_2$ and $Na_{0.55}MnO_2$ can be a significant source of the capacity fading in low potential operations observed in experiments. The evolution of the lattice parameters in an asymmetric manner in $Na_{0.44}MnO_2$ as a function of sodium intercalation/deintercalation is mainly due to the Jahn−Teller distortion. Our calculations further suggest that the substitution with Cr atoms without Jahn−Teller effects could reduce the volume change of $Na_{0.44}MnO_2$ significantly by about 50%.

■ ASSOCIATED CONTENT

Ⓢ Supporting Information

Migration energies of manganese atom, average distance between sodium ions, and the most stable structures for each composition. Oyxgen frameworks, SEM image. Calculated and measured XRD profiles. Structures and redox sequence for

transition metal substituted compounds (PDF).This material is available free of charge via the Internet at http://pubs.acs.org.

■ AUTHOR INFORMATION

Corresponding Author

*E-mail: ysjn@kaist.ac.kr, dkkim@kaist.ac.kr.

Notes

The authors declare no competing financial interest.

■ REFERENCES

(1) Komaba, S.; Nakayama, T.; Ogata, A.; Shimizu, T.; Takei, C.; Takada, S.; Hokura, A.; Nakai, I. *ECS Trans.* **2009**, *16*, 43.

(2) Kawabe, Y.; Yabuuchi, N.; Kajiyama, M.; Fukuhara, N.; Inamasu, T.; Okuyama, R.; Nakai, I.; Komaba, S. *Electrochem. Commun.* **2011**, *13*, 1225.

(3) Tripathi, R.; Ramesh, T.; Ellis, B. L.; Nazar, L. F. *Angew. Chem., Int. Ed.* **2010**, *122*, 8920.

(4) Trad, K.; Carlier, D.; Croguennec, L.; Wattiaux, A.; Ben Amara, M.; Delmas, C. *Chem. Mater.* **2010**, *22*, 5554.

(5) Hamani, D.; Ati, M.; Tarascon, J. M.; Rozier, P. *Electrochem. Commun.* **2011**, *13*, 938.

(6) Komaba, S.; Takei, C.; Nakayama, T.; Ogata, A.; Yabuuchi, N. *Electrochem. Commun.* **2010**, *12*, 355.

(7) Komaba, S.; Ishikawa, T.; Murata, W.; Yabuuchi, N.; Ozeki, T. *ECS Meeting Abstracts* **2010**, *1003*, 793.

(8) Komaba, S.; Nakayama, T.; Takei, C.; Yabuuchi, N.; Ogata, A.; Shimizu, T. *ECS Meeting Abstracts* **2010**, *1003*, 583.

(9) Cao, Y.; Xiao, L.; Wang, W.; Choi, D.; Nie, Z.; Yu, J.; Saraf, L. V.; Yang, Z.; Liu, J. *Adv. Mater.* **2011**, *23*, 3155.

(10) Sauvage, F.; Laffont, L.; Tarascon, J.-M.; Baudrin, E. *Inorg. Chem.* **2007**, *46*, 3289.

(11) Whitacre, J. F.; Tevar, a.; Sharma, S. *Electrochem. Commun.* **2010**, *12*, 463.

(12) Pauling, L. *J. Am. Chem. Soc.* **1929**, *51*, 1010.

(13) Ong, S. P.; Chevrier, V. L.; Hautier, G.; Jain, A.; Moore, C.; Kim, S.; Ma, X.; Ceder, G. *Energy Environ. Sci.* **2011**, *4*, 3680.

(14) Kresse, G. *Comput. Mater. Sci.* **1996**, *6*, 15.

(15) Blöchl, P. E. *Phys. Rev. B* **1994**, *50*, 17953.

(16) Perdew, J. P.; Burke, K.; Ernzerhof, M. *Phys. Rev. Lett.* **1996**, *77*, 3865.

(17) Dudarev, S. L.; Botton, G. A.; Savrasov, S. Y.; Humphreys, C. J.; Sutton, A. P. *Phys. Rev. B* **1998**, *57*, 1505.

(18) Wang, L.; Maxisch, T.; Ceder, G. *Phys. Rev. B* **2006**, *73*, 195107.

(19) Jain, A.; Hautier, G.; Moore, C. J.; Ping Ong, S.; Fischer, C. C.; Mueller, T.; Persson, K. a.; Ceder, G. *Comput. Mater. Sci.* **2011**, *50*, 2295.

(20) Stausholm-Møller, J.; Kristoffersen, H. H.; Hinnemann, B.; Madsen, G. K. H.; Hammer, B. *J. Chem. Phys.* **2010**, *133*, 144708.

(21) Monkhorst, H. J. *Phys. Rev. B* **1976**, *13*, 5188.

(22) Toukmaji, A. *Comput. Phys. Commun.* **1996**, *95*, 73.

(23) Zhang, X.; Tang, S.; Du, Y. *J. Phys. Chem. C* **2011**, *115*, 2644.

(24) Momma, K.; Izumi, F. *J. Appl. Crystallogr.* **2008**, *41*, 653.

(25) Parant, J. *J. Solid State Chem.* **1971**, *3*, 1.

(26) Mumme, W. G. *Acta Crystallogr., Sect. B* **1968**, *24*, 1114.

(27) Doeff, M. *J. Power Sources* **2004**, *135*, 240.

(28) Doeff, M. M.; Richardson, T. J.; Kepley, L. *J. Electrochem. Soc.* **1996**, *143*, 2507.

(29) Chu, Q.; Wang, X.; Li, Q.; Liu, X. *Acta Crystallogr., Sect. C* **2011**, *67*, i10.

(30) Kruk, I.; Zajdel, P.; van Beek, W. F.; Bakaimi, I.; Lappas, A.; Stock, C.; Green, M. A. *J. Am. Chem. Soc.* **2011**, *133*, 13950.

(31) Additional sodium sites that are marginally displaced near Na1 and Na3 positions in low temperature (5 K) synchrotron measurements are not identified in the present calculations due also to a limited cell size along the *c*-axis, since based on the experimental occupancies at 5 K, one would need a computationally unfeasibly large cell size with approximately 1000 atoms to fully identify all 8 sites.

(32) Paulsen, J. M. *J. Electrochem. Soc.* **1999**, *146*, 3560.

(33) Reed, J.; Ceder, G. *Chem. Rev.* **2004**, *104*, 4513.

(34) Burdett, J. K.; Price, G. D.; Price, S. L. *J. Am. Chem. Soc.* **1982**, *104*, 92.

(35) Saint, J. A.; Doeff, M. M.; Wilcox, J. *Chem. Mater.* **2008**, *20*, 3404.

(36) Meng, Y. S.; Van der Ven, A.; Chan, M.; Ceder, G. *Phys. Rev. B* **2005**, *72*, 172103.

(37) Aydinol, M.; Kohan, A.; Ceder, G.; Cho, K.; Joannopoulos, J. *Phys. Rev. B* **1997**, *56*, 1354.

(38) Rappe, A.; Casewit, C.; Colwell, K.; Goddard Iii, W.; Skiff, W. *J. Am. Chem. Soc.* **1992**, *114*, 10024.

(39) Peng, Z.; Ewig, C. S.; Hwang, M. J.; Waldman, M.; Hagler, A. T. *J. Phys. Chem. A* **1997**, *101*, 7243.

(40) Malik, R.; Zhou, F.; Ceder, G. *Nat. Mater.* **2011**, *10*, 587.

(41) Armstrong, A. R.; Huang, H.; Jennings, R. A.; Bruce, P. G. *J. Mater. Chem.* **1998**, *8*, 255.

(42) Goodenough, J. B.; Kim, Y. *Chem. Mater.* **2010**, *22*, 587.

(43) Armstrong, a. R.; Lyness, C.; Panchmatia, P. M.; Islam, M. S.; Bruce, P. G. *Nat. Mater.* **2011**, *10*, 223.

(44) Shin, Y.; Manthiram, A. *J. Electrochem. Soc.* **2004**, *151*, A204.

(45) Izumi, F.; Ikeda, T. *Mater. Sci. Forum* **2000**, *321−324*, 198.

(46) Chevrier, V.; Ong, S.; Armiento, R.; Chan, M.; Ceder, G. *Phys. Rev. B* **2010**, *82*, 075122.

(47) Gwon, H.; Seo, D.-H.; Kim, S.-W.; Kim, J.; Kang, K. *Adv. Funct. Mater.* **2009**, *19*, 3285.

(48) Burns, R. G. *Mineralogical Applications of Crystal Field Theory*; Cambridge University Press: 1993; Vol. 5.